#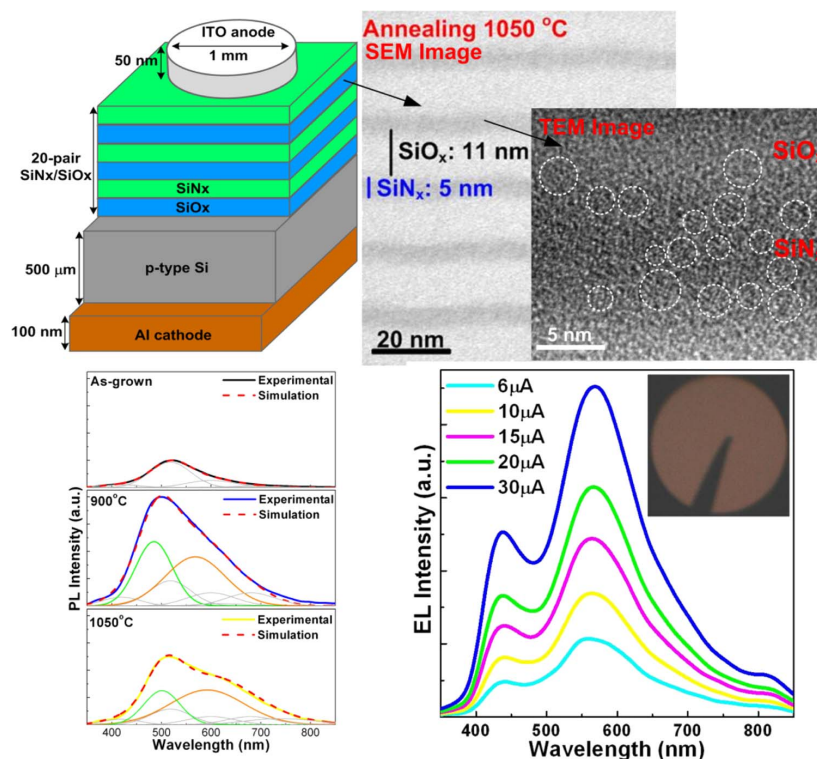 Wavelength-Shifted Yellow Electroluminescence of Si Quantum-Dot Embedded 20-Pair SiNx/SiOx Superlattice by Ostwald Ripening Effect

Hung-Yu Tai
Yung-Hsiang Lin
Gong-Ru Lin

Wavelength-Shifted Yellow Electroluminescence of Si Quantum-Dot Embedded 20-Pair SiNx/SiOx Superlattice by Ostwald Ripening Effect

Hung-Yu Tai, Yung-Hsiang Lin, and Gong-Ru Lin

Graduate Institute of Photonics and Optoelectronics, Department of Electrical Engineering, National Taiwan University, Taipei 106, Taiwan

Abstract: Yellow electroluminescence (EL) of a 20-pair Si-rich SiN$_x$/SiO$_x$ superlattice is demonstrated by plasma-enhanced chemical vapor deposition (PECVD) and annealing process. After annealing at 900 °C for 30 min, two photoluminescence (PL) peaks at 480 and 570 nm are observed to blue-shift the PL wavelength, and the corresponding peak intensity is enhanced due to the self-aggregation of Si quantum dots (QDs). When increasing the annealing temperature to 1050 °C, the PL peaks caused by the aggregated Si-QDs in SiN$_x$ and SiO$_x$ layers red-shift to 500 and 600 nm, thereby shifting the PL peak wavelength to 520 nm. Such a wavelength red-shifting phenomenon is mainly attributed to the formation of large Si-QDs due to the Ostwald ripening effect. The turn-on voltage and the V–I slope of the ITO/SiN$_x$/SiO$_x$/p-Si/Al LED device are 200 V and 15.5 kV/mA with Fowler–Nordheim (FN) tunneling assistant carrier transport under an effective barrier height of 1.3 eV. Maximum output-power–current slope of 0.2 μW/A at power conversion efficiency of 10^{-6} is detected.

Index Terms: Silicon nanophotonics, quantum dots (QDs) and single molecules, light-emitting diodes (LEDs), thin-film coatings.

1. Introduction

Nanoscale Si-based light source has emerged to impact the next-generation Si photonics because of their full compatibility with Si integrated-circuit (IC) technology. Researches on Si quantum dots (QDs) embedded in SiO$_x$/SiN$_x$/SiC$_x$ matrices are the key to overcoming the shortcoming of poor emission efficiency in bulk Si with indirect band-gap features [1]–[4]. Intensive visible photoluminescence (PL) and electroluminescence (EL) with ranked quantum efficiencies between 0.1%–8% [5]–[10] have ever been obtained by introducing the quantum confinement effect. Most past research emphasized characterizing single-layer Si-rich SiO$_x$ film with buried Si-QDs [11]–[17]. Multicolor Si-QDs embedded in SiO$_x$ film light-emitting diodes (LEDs) with improved emission efficiency are demonstrated by adjusting the Si-QD size from 4.1 to 1.8 nm [11]. Di *et al.* investigated boron-doped Si nanocrystal/c-Si p-n heterojunction LED with emission wavelengths ranging from visible to infrared regions [17]. A better host material, Si-rich SiN$_x$, has recently been considered to cause a wide tunable band gap from near infrared to UV regions (1.4 ∼ 3 eV), a low-energy barrier height (4.3 eV), and a small temperature-quenching effect [18]–[21]. Cen *et al.*
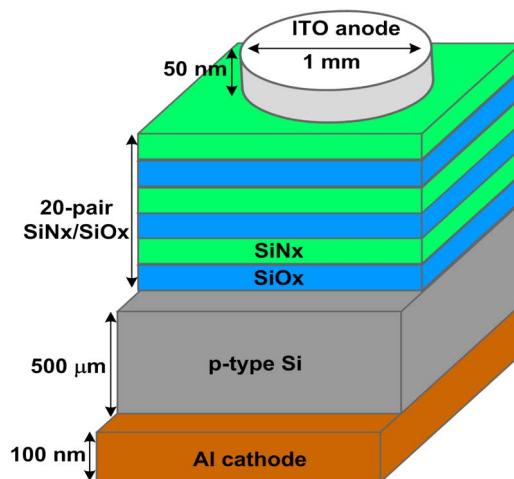
Fig. 1. Configuration of the 20-pair Si-rich SiN_x/SiO_x superlattice LED.

generated strong EL with tunable color from violet to white by using Si-implanted SiN_x thin films [22]. Later, the light emission efficiencies of the Si-QD-based LEDs were promoted through surface plasmons or surface roughness by using semiconductor or metal nanostructures. Lin *et al.* have introduced a surface nano-roughened Si substrate to enhance the external quantum efficiency by releasing the total reflection effect occurred at LED–air interface [23]. Huh *et al.* demonstrated the PL intensity enhancement of Si-QDs by employing Au nanoparticles [24]. Li *et al.* fabricated Ag island layer in the SiN_x LED to raise the injection current and the radiative efficiency. The EL intensity was enhanced by approximately 14 as compared with the SiN_x LED without the Ag island layer [25]. Wang *et al.* also showed an external quantum efficiency enhancement of the SiN_x LED through surface roughness by using the Ag island film [26]. Recently, a Si-based superlattice was proposed to control the size distribution and to promote the volume density of Si-QDs [27]. The lower interfacial barrier height facilitates carrier injection into Si-QDs from enhanced tunneling probability, which results in a high emission efficiency based on Fowler–Nordheim (FN) tunneling effect [19], [28]. The emission wavelength and emission efficiency of the Si-based superlattice LED depend on the size and the quantity of the Si-QD, which are influenced by the annealing conditions. Therefore, the relationship between the Si-QD formation and the annealing condition should be realized. With the induced Ostwald ripening effect occurring on the self-aggregated Si-QDs in this paper, the yellow EL of a 20-pair Si-rich SiN_x/SiO_x superlattice synsized by plasma-enhanced chemical vapor deposition (PECVD) is obtained through the aggregation of Si-QDs under precise annealing conditions. Both room-temperature PL and EL are analyzed to investigate the size confinement and efficiency enhancement of the Si-QDs embedded SiN_x/SiO_x superlattice LEDs.

2. Experimental Setup

The 20-pair Si-rich SiN_x/SiO_x superlattice was deposited on a (100)-oriented p-type Si substrate (thickness: 500 μm; resistivity: 10^{-3} Ω-cm) by PECVD with two reactant gas recipes of NH_3/SiH_4 for SiN_x synthesis and N_2O/SiH_4 for SiO_x synthesis at substrate temperature of 350 °C, in which the fluence ratios of NH_3/SiH_4 and N_2O/SiH_4 were set as 4 and 4.5, respectively. The plasma power and the chamber pressure were maintained at 80 W and 67 Pa during SiN_x and SiO_x growth. Thereafter, a transparent indium tin oxide (ITO)-based anode contact with a thickness of 50 nm was sputtered on the Si-rich SiN_x/SiO_x superlattice patterned with a photoresist, which was then dipped in acetone to form a pattern area of 0.25π mm^2 by the liftoff process. The bottom aluminum (Al) cathode with a thickness of 100 nm was evaporated to form a SiN_x/SiO_x superlattice LED; both the configuration and the device parameters of the SiN_x/SiO_x superlattice LED are shown in Fig. 1. The *I–V*, *P–I*, and EL characteristics were obtained under a forward bias by using a high voltage source
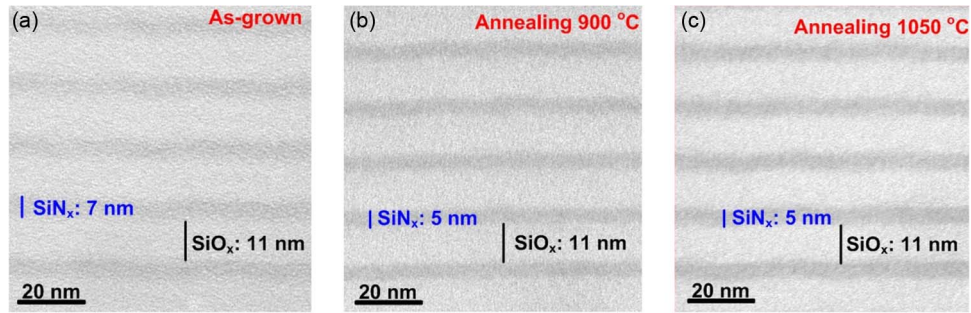
Fig. 2. TEM images of the 20- pair Si-rich SiN$_x$/SiO$_x$ superlattice samples. (a) as-grown sample, (b) annealed sample at 900 °C and (c) annealed sample at 1050 °C.
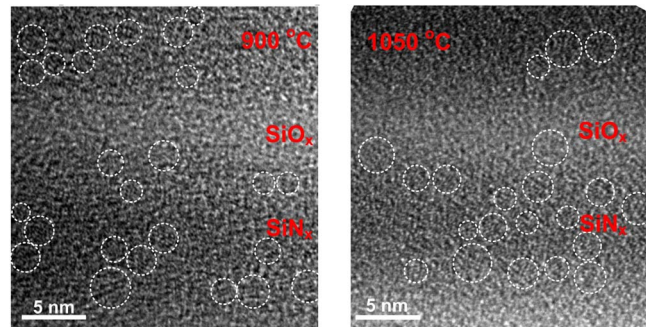

Fig. 3. TEM images of the Si-QD aggregation in the 20-pair Si-rich SiN$_x$/SiO$_x$ superlattice samples annealed at 900 °C (left) and 1050 °C (right) for 30 min.

(Keithley, SMU237) at room temperature. A monochromator (Spectral Products, DK240) combined with a photomultiplier tube (PMT, Hamamatsu 8250) was used as an optical spectrum analyzer to detect the EL response.

3. Results and Discussion

Fig. 2 shows the TEM images of the as-grown and annealed 20-pair Si-rich SiN$_x$/SiO$_x$ superlattice samples. The thicknesses of the as-grown Si-rich SiN$_x$ and SiO$_x$ layers are 7 and 11 nm, respectively. After annealing at 900 °C and 1050 °C for 30 min, the SiN$_x$ layer becomes dense with its thickness reducing to 5 nm, whereas the SiO$_x$ layer thickness stays constant at 11 nm. Fig. 3 shows the TEM images of the Si-QD aggregation in the superlattice samples annealed at 900 °C (left) and 1050 °C (right) for 30 min. Fig. 4 demonstrates the Si-QD size distributions of the annealed super-lattice samples. For the annealed samples at 900 °C, the Si-QD size in the SiN$_x$ layer is approximately 1.7 $\pm$ 0.3 nm. The Si-QD size in the SiO$_x$ layer is approximately 2.5 $\pm$ 0.4 nm. By increasing the annealing temperature to 1050 °C, the Si-QD size in the SiN$_x$ layer is approximately 1.75 $\pm$ 0.4 nm, and the Si-QD size in the SiO$_x$ layer is approximately 2.8 $\pm$ 0.5 nm. The density of Si-QDs in the SiN$_x$ film is larger than that in the SiO$_x$ film because N ions are less reactant with Si atoms than the O ions to facilitate the formation of stable Si-SiN$_x$ interfaces [29].

Fig. 5(a) and (b) show the X-ray photoelectron spectroscopy (XPS) images of the as-grown Si-rich SiN$_x$ and SiO$_x$ films, respectively. For the SiN$_x$ film, the Si$_{2p}$ line and the N$_{1s}$ line are located at 102 and 398. 4 eV, respectively [30]. The composition ratio of N/Si is determined as 1.02. For the SiO$_x$ film, the Si$_{2p}$ line and the O$_{1s}$ line are located at 106.3 and 536 eV, respectively [31]. The composition ratio is determined as 1.55. The composition ratios of SiN$_x$ and SiO$_x$ films remain unchanged after annealing process. According to the theoretical model, the composition ratios of SiN$_x$ and SiO$_x$ films determine the diffusion coefficient, which significantly affect the sizes of
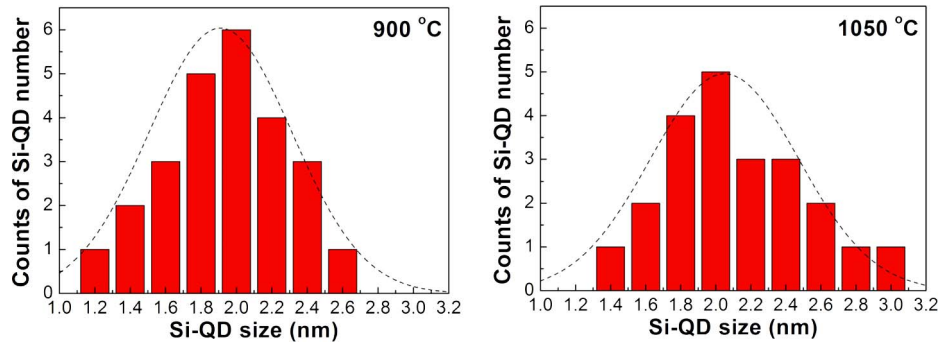
Fig. 4. Size distributions of Si-QD in the Si-rich SiN$_x$/SiO$_x$ superlattice samples annealed at (left) 900 °C and (right) 1050 °C for 30 min.
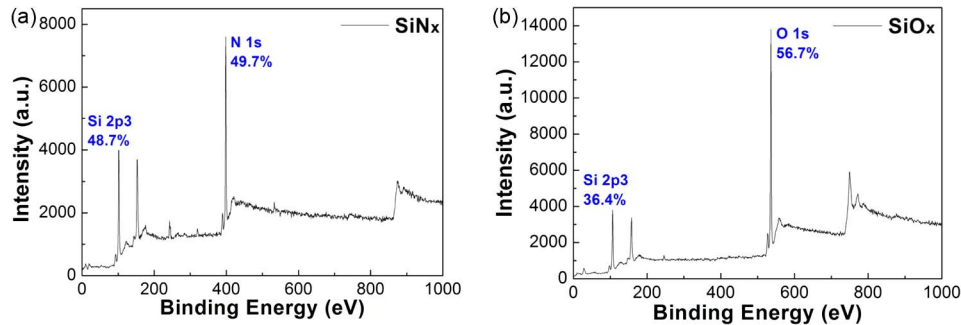

Fig. 5. (a) The XPS of the as-grown Si-rich SiN$_x$ film. (b) The XPS of the as-grown Si-rich SiO$_x$ film.

Si-QDs [31]. The excessive Si atoms self-aggregate into Si-QDs after annealing process. Increases in the quantity of excessive Si atoms can enlarge the size of the Si-QD.

In PL analysis, the He–Cd laser at 325 nm with a 40-mW output was utilized as the pumping source. Fig. 6(a) demonstrates the PL spectra of the as-grown and annealed 20-pair Si-rich SiN$_x$/SiO$_x$ superlattice samples. The deconvoluted signals caused by defects and Si-QDs are generated by Gaussian functions. The dashed lines shown in Fig. 6(a) are the simulated curves of the PL spectra, which are the integrations of the deconvoluted PLs. For the as-grown 20-pair Si-rich SiN$_x$/SiO$_x$ superlattice sample, the PL spectrum is induced by the localized tail states [32], [33]. Fig. 6(b) shows the deconvoluted signals caused by defects and Si-QDs of the 20-pair Si-rich SiN$_x$/SiO$_x$ superlattice samples. The deconvoluted PL signals of the annealed samples located at 480 (green line) and 570 nm (orange line) are attributed to the aggregations of Si-QDs. Except for these two signals, the luminescences caused by the defect states are shown as the gray lines. The PL peaks located at 420 and 520 nm originate from the weak oxygen bond (WOB) defect and the radiative Si dangling bond center [34]–[36]. The PL peaks at 600 and 622 nm are attributed to the nonbridging oxygen hole center (NBOHC) and the silicon defect states ($\equiv$ Si^0) [34], [37]. In addition, the nitrogen defect state (N$_2^0$) in the SiN$_x$ layer generates the PL with peak wavelength at 680 nm [38]. Fig. 6(c) only demonstrates the deconvoluted PL signals caused by the defects states. After the annealing process, the deconvoluted PL signals caused by the defect states of the annealed samples remain the same peak wavelength and linewidth as compared with the as-grown sample.

Two PL peaks at 480 and 570 nm are obviously observed after annealing at 900 °C for 30 min. Therefore, the integrated PL peak is blue-shifted to 500 nm, and the peak intensity is enhanced as compared with the as-grown sample. This wavelength blue-shifting phenomenon and the peak intensity enhancement are attributed to the quantum confinement effect of the Si-QDs aggregation in the annealed samples [29]. The formations of Si-QD can be investigated by the TEM images as
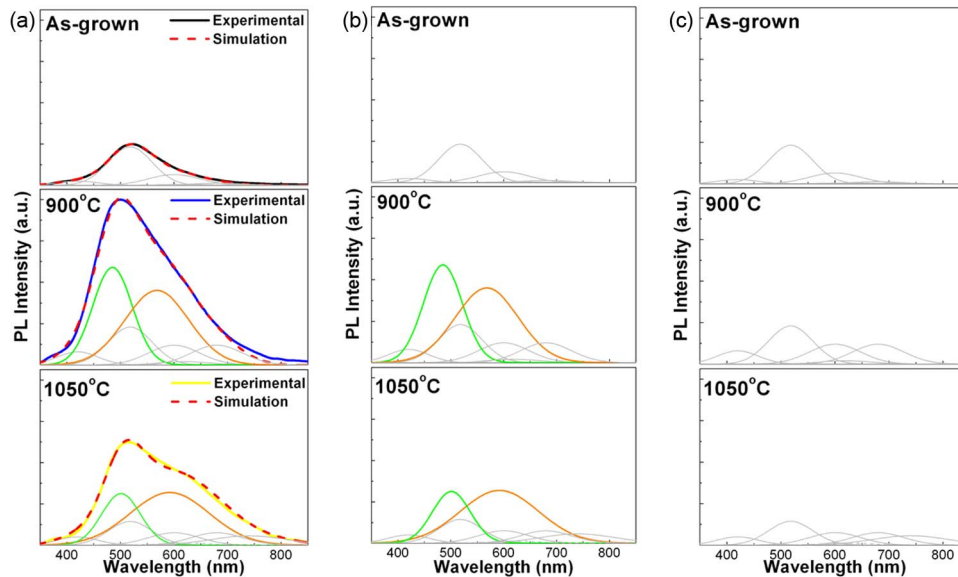
Fig. 6. (a) The PL spectra of the as-grown and the annealed 20-pair Si-rich SiN$_x$/SiO$_x$ superlattice samples. (b) The deconvoluted PL spectra of the as-grown and the annealed 20-pair Si-rich SiN$_x$/SiO$_x$ superlattice samples. (c) The deconvoluted PL spectra for showing the defect states induced PL responses.

shown in Fig. 2. For the annealed samples at 900 °C, the Si-QD size in SiN$_x$ layer is 1.7 ± 0.3 nm. Park *et al.* showed that a peak wavelength of 500 nm corresponds to the Si-QD size of 1.6 nm [39]. This theoretical result is derived from $E_g(\mathrm{eV}) = 1.56 + 2.4/d^2$, where E denotes the peak energy, and d denotes the Si-QD size in the SiN$_x$ film [39]. The Si-QD size in the SiO$_x$ layer is 2.5 ± 0.4 nm. The corresponding peak wavelength is 570 nm, which correlates well with the theoretical value of 2.6 nm obtained from $E_g(\mathrm{eV}) = 1.12 + 5.83/d^{1.78}$ [40]. Consequently, the PL signal located at 480 nm is attributed to the aggregation of Si-QDs in SiN$_x$ layer. In contrast, the PL signal at 570 nm is caused by the aggregation of Si-QDs in the SiO$_x$ layer.

After annealing up to 1050 °C, the PL peaks caused by the aggregation of Si-QDs in the SiN$_x$ and the SiO$_x$ layers red-shift to 500 nm (from 480 nm) and 600 nm (from 570 nm), thereby shifting the integrated PL peak to 520 nm. Such a wavelength red-shifting phenomenon is caused by the formations of large Si-QD [41]. The Si-QD size in SiN$_x$ layer is 1.75 ± 0.4 nm, and the Si-QD size in SiO$_x$ layer is 2.8 ± 0.5 nm. Generally, the emission wavelength depends strictly on the Si-QD size and can be easily detuned from 400 to 700 nm to deliver blue and red light with corresponding Si-QD size ranging between 1.5 and 4.5 nm [32]. Typically, the quantum confinement effect has less of an influence when the Si-QD size exceeds 5 nm. The PL intensity I_{PL} is proportional to the density of Si-QDs with $I_{PL} \propto N\sigma\tau/\tau_r$, where N denotes the total luminescence center (Si-QD), σ represents the cross section, and τ and τ_r represent the lifetime and the radiative lifetime, respectively [41]. The increasing temperature leads to a large Si-QD formation and a decreasing number of Si-QD caused by the Ostwald ripening phenomena. When increasing the annealing temperature, the free Si atoms tend to precipitate on large Si-QD surface, whereas small Si-QD may also redeposit onto the large surfaces. Eventually, the small Si-QDs shrink, and the large Si-QDs grows; the relation between the mean radius r and the annealing time t is written by $r^3 \propto t$ [41]. Consequently, the attenuated PL response red-shifts its peak wavelength by enlarging the diameter and reducing the density of Si-QDs after experiencing a higher annealing temperature, as shown in Fig. 6. These results can be used to interpret the reduced PL intensity and the broadened PL linewidth.

The ITO/SiN$_x$/SiO$_x$ superlattice/p-Si/Al light-emitting device was fabricated by the sputtering system and thermal evaporation coater. The electrical properties were investigated by the *I–V* curves, *P–I* curves, and EL spectrum. Fig. 7 shows the *I–V* curve of the SiN$_x$/SiO$_x$ superlattice sample annealed at 1050 °C for 30 min. The turn-on voltage and the *V–I* slope are 200 V and
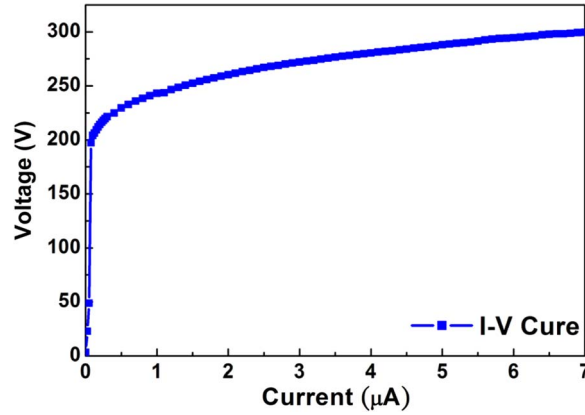
Fig. 7. I–V curve of the ITO/SiN$_x$/SiO$_x$ superlattice/p-Si/Al light-emitting device.

15.5 kV/mA, respectively. The FN tunneling effect is utilized to analyze the carrier transport mechanism and fit the experimental data. The analytical equations are provided below. The transmission $t(E_x)$ is a function of an energy E_x incident at the barrier of the interface, as given by the following equation:

$$t(E_x) = \exp\left\{ -2 \int_{x_{ti}}^{x_{tx}} \left(\frac{2m_{ox}}{\eta^2}\right)^{1/2} \left[(q\Psi(x) - E_x)^{1/2}\right] dx \right\} \qquad (1)$$

where m_{ox} denotes the effective mass of an electron, $q\Psi(x)$ is the potential barrier, q is the electron charge, and $x_{tx} - x_{ti}$ is the tunnel distance. After integrating all possible energies by using the Wentzel–Kramers–Brillouin (WKB) approximation, in the absence of Schottky effect with $x_{ti} = 0$ Å (ignoring temperature variation and barrier shrinkage), the FN tunneling current density J_{F-N} can be expressed as [8], [19], [42], [43]

$$J_{F-N} = \frac{4\pi q m_0}{\eta^3} \int_{E_x} t(E_x) dE_x \int_{E_x}^{+\infty} f(E_x, T) dE = \frac{q^3(m_0/m_{ox})}{8\pi h \phi_B} E^2 \exp\left(-\frac{8\pi\sqrt{2m_{ox}\phi_B^3}}{3qhE}\right)$$

$$= 1.54 \times 10^{-6} \frac{(m_0/m_{ox})}{\phi_B} E^2 \exp\left(-6.83 \times 10^7 \frac{\sqrt{2(m_{ox}/m_0)/\phi_B^3}}{E}\right) \qquad (2)$$

where m_0 is the free electron mass, m_{ox} is the effective mass of electron, T is the temperature, $f(E_x, T)$ is the Fermi–Dirac function, E is the electric field in SiO$_x$ and SiN$_x$ layer, and ϕ_B is the effective barrier height. By considering the current density, (2) can be transferred to

$$\ln\left(\frac{J_{FN}}{E^2}\right) = \ln\left(\frac{1.54 \times 10^{-6} m}{m_{ox}\phi_B^2}\right) - 6.83 \times 10^7 \frac{\sqrt{2(m_{ox}/m)}\phi_B^3}{E}. \qquad (3)$$

Fig. 8 shows the linear relation between $\ln(J_{FN}/E^2)$ and $1/E$ by using (3). Considering that the effective mass is 0.5 times smaller than the free electron mass, the effective barrier height ϕ_B is 1.31 eV, which is obtained by calculating the slope. This value is lower than 2.0 eV (the barrier height of pure Si$_3$N$_4$ [44]) because of the carrier injection enhancement in Si-QDs caused by the superlattice structure. The turn-on voltage exceeds over 200 V because the carrier transport in the highly resistive SiN$_x$ and SiO$_x$ layers still relies on the FN tunneling process. The series resistance of the SiN$_x$/SiO$_x$ superlattice LED is extremely large due to the insulating properties of the superlattice based on stacked SiN$_x$ and SiO$_x$ layers. It is clearly shown in Fig. 8 that the turn-on of the SiN$_x$/SiO$_x$ superlattice LED is occurred at 1×10^7 V/cm, corresponding to a voltage up to
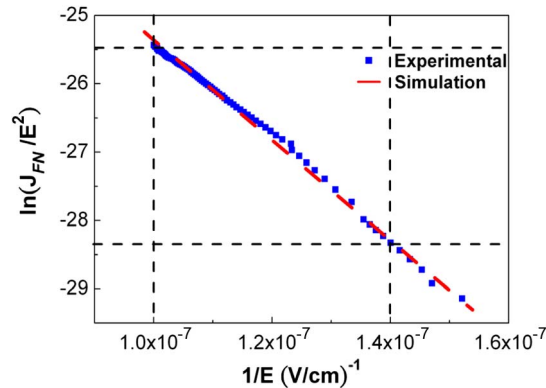
Fig. 8. $\ln(J_{FN}/E^2)$ as a function of 1/E in the ITO/ SiN_x/SiO_x superlattice/p-Si/Al light-emitting device.
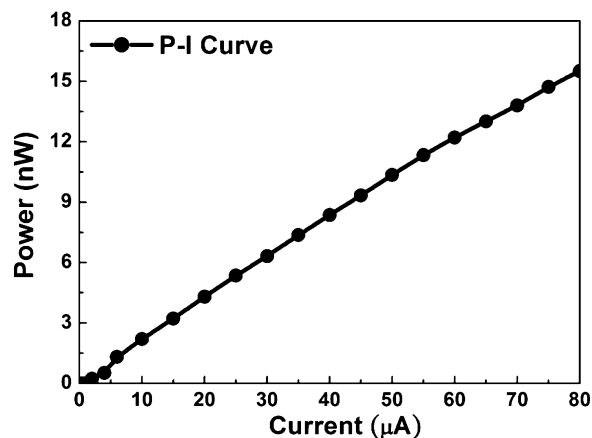

Fig. 9. P-I curve of the ITO/SiN_x/SiO_x superlattice/p-Si/Al LED.

200–250 V for the sample with an active layer thickness of 250 nm. In practical, it is necessary to decrease the series resistance or to change the carrier transport mechanism of the SiN_x/SiO_x superlattice with reduced thickness. Using SiN or SiC matrix with lower barrier height in the superlattice sample could also decrease the effective barrier height and reduce the turn-on voltage.

The $P–I$ curve of the electronic device under forward bias at room temperature is shown in Fig. 9. The maximum output power and the $P–I$ slope are 15.5 nW and 0.2 μW/A, respectively. Based on the $P–I$ and the $I–V$ curve, the power conversion efficiency (PCR) is about 1×10^{-6} by calculating the ratio of the output optical power to the input electrical power ($P_{out}/I_{bias} V_{bias}$). By using this super-lattice device, the effective barrier height is reduced to facilitate the enhancement of electron–hole pair recombination in the Si-QDs. The EL performances of the ITO/SiN_x/SiO_x superlattice/p-type Si/Al electric device with bias current injection from 6 to 30 μA and applied voltages of 295 V are shown in Fig. 10. The peak at 570 nm dominates, and the other peak at 435 nm is also observed. The peak intensity at 570 nm is increased four times with bias current injection from 6 to 30 μA and light emission is uniform when observing the inset of EL pattern in Fig. 10. The EL intensity is linearly proportional to the injected current; such phenomenon interprets that the EL of the device is dominated by the electron–hole pair recombination in the Si-QD rather than the impact ionization process. If the impact ionization process occurs, the broader EL linewidth and the changed EL intensity can be observed [3].

Fig. 11 demonstrates the PL and EL spectra of the 20-pair Si-rich SiN_x/SiO_x superlattice samples annealed at 1050 °C for 30 min. The deconvoluted signals in the PL and EL spectra are generated by Gaussian functions. The dashed lines are the simulated curves of the PL and EL spectra, which
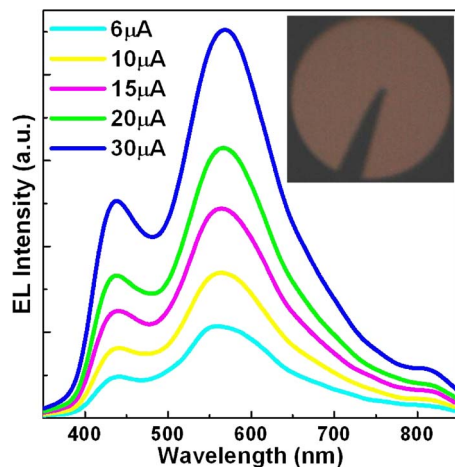
Fig. 10. EL of the ITO/SiN$_x$/SiO$_x$ superlattice/p-Si/Al light-emitting device with a picture of EL pattern.
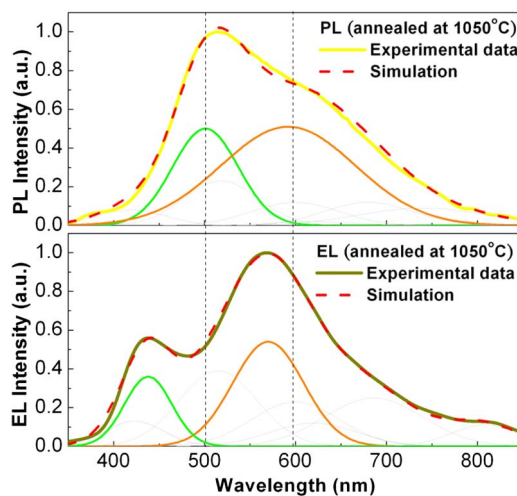

Fig. 11. Deconvoluted PL and EL of the annealed 20-pair Si-rich SiN$_x$/SiO$_x$ superlattice samples.

are the integrations of the deconvoluted signals. After deconvolution, the principle EL peak induced by the Si-QDs in SiO$_x$ layer is centered at 563 nm (orange line). Simultaneously, the secondary EL peak induced by the smaller Si-QDs in SiN$_x$ layer is centered at 437 nm (green line). In this case, the device is operated under a high applied voltage, thereby increasing the energy of the injected carrier to excite the small Si-QD [3]. The deviated EL peak wavelength also results from the tunneling of accumulated minority holes in the ground states of defects at high bias voltage. These radiative defects related EL obtained in the soft-breakdown condition can be greatly enlarged because of the bending band structure of Si-QD near the SiO$_x$/Si interface [33]. As a result, the EL peak at 435 nm is the combined PL response from the WOB defect and the Si-QDs in SiN$_x$ layer.

4. Conclusion

In conclusion, the 20-pair Si-rich SiN$_x$/SiO$_x$ superlattice structure has been deposited by PECVD with NH$_3$/SiH$_4$ and N$_2$O/SiH$_4$ reactant gas and annealing process. The thickness of the as-grown Si-rich SiN$_x$ and SiO$_x$ layers is 7 and 11 nm, respectively. After annealing at 900 °C and 1050 °C for 30 min, the SiN$_x$ layer becomes dense with its thickness reducing to 5 nm, whereas the SiO$_x$ layer thickness keeps constant at 11 nm by observing the HRTEM images. For the annealed samples at

900 °C, the Si-QD size in the SiN$_x$ layer is approximately 1.7 $\pm$ 0.3 nm. The Si-QD size in the SiO$_x$ layer is approximately 2.5 $\pm$ 0.4 nm. Increasing the annealing temperature to 1050 °C, the Si-QD size in the SiN$_x$ layer is approximately 1.75 $\pm$ 0.4 nm, and the Si-QD size in the SiO$_x$ layer is approximately 2.8 $\pm$ 0.5 nm. The PL of the as-grown sample caused by the defect states is demonstrated. After annealing at 900 °C for 30 min, two PL peaks at 480 nm and 570 nm have been observed to blue-shift the PL wavelength, and the peak intensity has been enhanced due to the aggregation of Si-QDs. When increasing the annealing temperature to 1050 °C, the PL peaks caused by the aggregation of Si-QDs in the SiN$_x$ and the SiO$_x$ layers red-shift to 500 nm and 600 nm, thereby shifting the integrated PL peak to 520 nm. Such a wavelength red-shifting phenomenon is caused by the formations of large Si-QD. As increasing the temperature, the small QDs shrink and the large QDs enlarge the size due to Ostwald ripening phenomena, which results in a growth of the mean radius and the increasing size distribution. Therefore, the PL peak red-shifts and the PL FWHM broadens. The turn-on voltage and the V–I slope of the ITO/SiN$_x$/SiO$_x$ superlattice/p-Si/Al LED device are 200 V and 15.5 kV/mA. The carrier transport mechanism is dominated by FN tunneling. The effective barrier height is 1.3 eV due to the carrier injection enhancement in Si-QD. The maximum output power and the P–I slope are 15.5 nW and 0.2 μW/A, respectively. Based on the P–I and I–V curves, the PCR is determined as 1×10^{-6}. The EL peak wavelength is slightly deviated because the carrier is preferred to inject into small Si-QD under high applied voltage. The EL intensity is enlarged linearly with increasing current injection, which interprets that the EL of the device is dominated by the electron–hole pair recombination in the Si-QD.

References

[1] L. Pavesi, L. Dal Negro, C. Mazzoleni, G. Franzo, and F. Priolo, "Optical gain in silicon nanocrystals," *Nature*, vol. 408, no. 6811, pp. 440–444, Nov. 2000.

[2] G.-R. Lin, C.-J. Lin, C.-K. Lin, L. J. Chou, and Y.-L. Chueh, "Oxygen defect and Si nanocrystal dependent white-light and near-infrared electroluminescence of Si-implanted and plasma-enhanced chemical-vapor deposition-grown Si-rich SiO$_2$," *J. Appl. Phys.*, vol. 97, no. 9, p. 094306, May 2005.

[3] K. S. Cho, N. M. Park, T. Y. Kim, K. H. Kim, and G. Y. Sung, "High efficiency visible electroluminescence from silicon nanocrystals embedded in silicon nitride using a transparent doping layer," *Appl. Phys. Lett.*, vol. 86, no. 7, p. 071909, Feb. 2005.

[4] C.-H. Cheng, C.-L. Wu, C.-C. Chen, L.-H. Tsai, Y.-H. Lin, and G.-R. Lin, "Si-rich Si$_x$C$_{1-x}$ light-emitting diodes with buried Si quantum dots," *IEEE Photon. J.*, vol. 4, no. 5, pp. 1762–1775, Oct. 2012.

[5] N. Lalic and J. Linnros, "Characterization of a porous silicon diode with efficient and tunable electroluminescence," *J. Appl. Phys.*, vol. 80, no. 10, pp. 5971–5977, Nov. 1996.

[6] K. Nishimura, Y. Nagao, and N. Ikeda, "High external quantum efficiency of electroluminescence from photoanodized porous silicon," *Jpn. J. Appl. Phys. 2, Lett.*, vol. 37, pp. L303–L305, 1998.

[7] B. Gelloz and N. Koshida, "Electroluminescence with high and stable quantum efficiency and low threshold voltage from anodically oxidized thin porous silicon diode," *J. Appl. Phys.*, vol. 88, no. 7, pp. 4319–4324, Oct. 2000.

[8] G.-R. Lin, C.-J. Lin, and H.-C. Kuo, "Improving carrier transport and light emission in a silicon-nanocrystal based MOS light-emitting diode on silicon nanopillar array," *Appl. Phys. Lett.*, vol. 91, no. 9, p. 093122, Aug. 2007.

[9] A. Marconi, A. Anopchenko, M. Wang, G. Pucker, P. Bellutti, and L. Pavesi, "High power efficiency in Si-NC/SiO$_2$ multilayer light emitting devices by bipolar direct tunneling," *Appl. Phys. Lett.*, vol. 94, no. 22, p. 221110, Jun. 2009.

[10] K. Y. Cheng, R. Anthony, U. R. Kortshagen, and R. J. Holmes, "High-efficiency silicon nanocrystal light-emitting devices," *Nano Lett.*, vol. 11, no. 5, pp. 1952–1956, May 2011.

[11] B. H. Lai, C. H. Cheng, and G.-R. Lin, "Multicolor ITO/SiO$_x$/p-Si/Al light emitting diodes with improved emission efficiency by small Si quantum dots," *IEEE J. Quantum Electron.*, vol. 47, no. 5, pp. 698–704, May 2011.

[12] D. Riabinina, C. Durand, M. Chaker, and F. Rosei, "Photoluminescent silicon nanocrystals synthesized by reactive laser ablation," *Appl. Phys. Lett.*, vol. 88, no. 7, p. 073105, Feb. 2006.

[13] I. Umezu, K. Yoshida, A. Sugimura, T. Inokuma, S. Hasegawa, Y. Wakayama, Y. Yamada, and T. Yoshida, "A comparative study of the photoluminescence properties of a-SiO$_x$:H film and silicon nanocrystallites," *J. Non-Cryst. Solids*, vol. 266–269, pp. 1029–1032, 2000.

[14] C. Huh, J. H. Shin, K. H. Kim, C. J. Choi, K. S. Cho, J. Hong, and G. Y. Sung, "Enhancement of performance of Si nanocrystal light-emitting diodes by using Ag nanodots," *IEEE Photon. Technol. Lett.*, vol. 18, no. 19, pp. 2068–2070, Oct. 1, 2006.

[15] D. Comedi, O. H. Y. Zalloum, J. Wojcik, and P. Mascher, "Light emission from hydrogenated and unhydrogenated Si-nanocrystal/Si dioxide composites based on PECVD-grown Si-rich Si oxide films," *IEEE J Sel. Topics Quantum. Electron.*, vol. 12, no. 6, pp. 1561–1569, Nov./Dec. 2006.

[16] C.-J. Lin and G.-R. Lin, "Enhancing nanocrystallite Si electroluminescence by suppressing oxygen decomposition in high-temperature and low-plasma-power PECVD," *J. Electrochem. Soc.*, vol. 154, no. 8, pp. H743–H748, 2007.

[17] D. Di, I. Perez-Wurfl, L. Wu, Y. Huang, A. Marconi, A. Tengattini, A. Anopchenko, L. Pavesi, and G. Conibeer, "Electroluminescence from Si nanocrystal/c-Si heterojunction light-emitting diodes," *Appl. Phys. Lett.*, vol. 99, no. 25, p. 251113, Dec. 2011.

[18] Y. H. Lin, C. L. Wu, Y. H. Pai, and G.-R. Lin, "A 533-nm self-luminescent Si-rich SiN$_x$/SiO$_x$ distributed Bragg reflector," *Opt. Exp.*, vol. 19, pp. 6563–6570, 2011.

[19] C. Huh, K. H. Kim, B. K. Kim, W. Kim, H. Ko, C. J. Choi, and G. Y. Sung, "Enhancement in light emission efficiency of a silicon nanocrystal light-emitting diode by multiple-luminescent Structures," *Adv. Mater.*, vol. 22, no. 44, pp. 5058–5062, Nov. 2010.

[20] C. Jiang and M. A. Green, "Silicon quantum dot superlattices: Modeling of energy bands, densities of states, and mobilities for silicon tandem solar cell applications," *J. Appl. Phys.*, vol. 99, no. 11, p. 114902, Jun. 2006.

[21] J. Warga, R. Li, S. N. Basu, and L. D. Negro, "Electroluminescence from silicon-rich nitride/silicon superlattice structures," *Appl. Phys. Lett.*, vol. 93, no. 15, p. 151116, Oct. 2008.

[22] Z. H. Cen, T. P. Chen, L. Ding, Z. Liu, J. I. Wong, M. Yang, W. P. Goh, and S. Fung, "Influence of implantation dose on electroluminescence from Si-implanted silicon nitride thin films," *Appl. Phys. A, Mater. Sci. Process.*, vol. 104, no. 1, pp. 239–245, Jul. 2011.

[23] G.-R. Lin, Y.-H. Pai, and C.-T. Lin, "Microwatt MOSLED using SiO$_x$ with buried Si nanocrystals on Si nano-pillar array," *J. Lightw. Technol.*, vol. 26, no. 11, pp. 1486–1491, Jun. 2008.

[24] C. Huh, C. J. Choi, W. Kim, B. K. Kim, B. J. Park, E. H. Jang, S. H. Kim, and G. Y. Sung, "Enhancement in light emission efficiency of Si nanocrystal light-emitting diodes by a surface plasmon coupling," *Appl. Phys. Lett.*, vol. 100, no. 18, p. 181108, Apr. 2012.

[25] D. Li, F. Wang, C. Ren, and D. Yang, "Improved electroluminescence from silicon nitride light emitting devices by localized surface plasmons," *Opt. Exp.*, vol. 2, no. 6, pp. 872–877, Jun. 2012.

[26] F. Wang, D. Li, D. Yang, and D. Que, "Enhancement of light-extraction efficiency of SiN$_x$ light emitting devices through a rough Ag island film," *Appl. Phys. Lett.*, vol. 100, no. 3, p. 031113, Jan. 2012.

[27] S. Huang, H. Xiao, and S. Shou, "Annealing temperature dependence of Raman scattering in Si/SiO$_2$ superlattice prepared by magnetron sputtering," *Appl. Surf. Sci.*, vol. 255, no. 8, pp. 4547–4550, Feb. 2009.

[28] G.-R. Lin, C.-J. Lin, and C.-K. Lin, "Enhanced Fowler–Nordheim tunneling effect in nanocrystallite Si based LED with interfacial Si nano-pyramids," *Opt. Exp.*, vol. 15, no. 5, pp. 2555–2563, Mar. 2007.

[29] Y. Q. Wang, Y. G. Wang, L. Cao, and Z. X. Cao, "High-efficiency visible photoluminescence from amorphous silicon nanoparticles embedded in silicon nitride," *Appl. Phys. Lett.*, vol. 83, no. 17, pp. 3474–3476, Oct. 2003.

[30] S. P. Singh, P. Srivastava, S. Ghosh, S. A. Khan, and G. V. Prakash, "Phase stabilization by rapid thermal annealing in amorphous hydrogenated silicon nitride film," *J. Phys. Condens. Matter*, vol. 21, no. 9, p. 095010, Mar. 2009.

[31] G.-R. Lin, T. C. Lo, L. H. Tsai, Y. H. Pai, C. H. Cheng, C. I. Wu, and P. S. Wang, "Finite silicon atom diffusion induced size limitation on self-assembled silicon quantum dots in silicon-rich silicon carbide," *J. Electrochem. Soc.*, vol. 159, no. 2, pp. K35–K41, 2012.

[32] F. Giorgis, P. Mandracci, L. Dal Negro, C. Mazzoleni, and L. Pavesi, "Optical absorption and luminescence properties of wide-bandgap amorphous silicon based alloys," *J. Non-Cryst. Solids*, vol. 266–269, pp. 588–592, May 2000.

[33] J. Kistner, X. Chen, Y. Weng, H. P. Strunk, M. B. Schubert, and J. H. Werner, "Photoluminescence from silicon nitride—No quantum effect," *J. Appl. Phys.*, vol. 110, no. 2, p. 023520, Jul. 2011.

[34] C. J. Lin and G.-R. Lin, "Defect-enhanced visible electroluminescence of multi-energy silicon-implanted silicon dioxide film," *IEEE J. Quantum Electron.*, vol. 41, no. 3, pp. 441–447, Mar. 2005.

[35] M. Wang, D. Li, Z. Yuan, D. Yang, and D. Que, "Photoluminescence of Si-rich silicon nitride: Defect-related states and silicon nanoclusters," *Appl. Phys. Lett.*, vol. 90, no. 13, p. 131903, Mar. 2007.

[36] M. Wang, J. Huang, Z. Yuan, A. Anopchenko, D. Li, D. Yang, and L. Pavesi, "Light emission properties and mechanism of low-temperature prepared amorphous SiN$_x$ films. II. Defect states electroluminescence," *J. Appl. Phys.*, vol. 104, no. 8, p. 083505, Oct. 2008.

[37] Z. H. Cen, T. P. Chen, L. Ding, Y. Liu, J. I. Wong, M. Yang, Z. Liu, W. P. Goh, F. R. Zhu, and S. Fung, "Evolution of electroluminescence from multiple Si-implanted silicon nitride films with thermal annealing," *J. Appl. Phys.*, vol. 105, no. 12, p. 123101, Jun. 2009.

[38] A. Zerga, M. Carrada, M. Amann, and A. Slaoui, "Si-nanostructures formation in amorphous silicon nitride SiN$_x$:H deposited by remote PECVD," *Phys. E, Low-Dimensional Syst. Nanostruct.*, vol. 38, no. 1/2, pp. 21–26, Apr. 2007.

[39] N. M. Park, C. J. Choi, T. Y. Seong, and S. J. Park, "Quantum confinement in amorphous silicon quantum dots embedded in silicon nitride," *Phys. Rev. Lett.*, vol. 86, no. 7, pp. 1355–1357, Feb. 2001.

[40] C. L. Wu and G.-R. Lin, "Power gain modeling of Si quantum dots embedded SiO$_x$ waveguide amplifier with inhomogeneous broadened spontaneous emission," *IEEE J. Sel. Topics Quantum. Electron.*, 2012, to be published.

[41] F. Iacona, C. Bongiorno, C. Spinella, S. Boninelli, and F. Priolo, "Formation and evolution of luminescent Si nano-clusters produced by thermal annealing of SiO$_x$ films," *J. Appl. Phys.*, vol. 95, no. 7, pp. 3723–3722, Apr. 2004.

[42] M. Lenzlinger and E. H. Snow, "Fowler–Nordheim tunneling into thermally grown SiO$_2$," *J. Appl. Phys.*, vol. 40, no. 1, pp. 278–283, Jan. 1969.

[43] R. H. Fowler and L. Nordheim, "Electron emission in intense electric fields," *Proc. R. Soc. Lond. A, Math. Phys. Char.*, vol. 119, no. 781, pp. 173–181, May 1928.

[44] J. Chan, H. Wong, M. C. Poon, and C. W. Kok, "Oxynitride gate dielectric prepared by thermal oxidation of low-pressure chemical vapor deposition silicon-rich silicon nitride," *Microelectron. Reliab.*, vol. 43, no. 4, pp. 611–616, Apr. 2003.